**ROYAL SOCIETY OF CHEMISTRY**

## PAPER

Check for updates

# *Operando* phase transition mapping of the negative electrode of a Li-ion 18 650 battery at high C-rates through fast synchrotron XRD-CT measurements†

I. Mombrini,[ac] T. M. M. Heenan,[ab] S. Checchia,[c] Anmol Jnawali,[ab] C. Tan,[ab] M. J. Johnson,[a] M. Di Michiel,[c] R. Jervis,[abe] A. J. E. Rettie,[abe] D. J. L. Brett[ab] and P. R. Shearing ★[abd]

Lithium-ion batteries (LIBs) have become indispensable in everyday devices and are now being widely used in electric vehicles (EVs) due to their high energy density and long cycle life. However, these batteries are not without their limitations and face various degradation mechanisms that can impact their performance and safety. As the demand for more reliable and efficient batteries grows, it becomes crucial to understand these degradation mechanisms and develop strategies for improving the design and operation of LIBs. Therefore, degradation mechanisms have to be investigated to improve and re-design the commercial devices with the goal of enhancing their capacity, improving their safety and performances. Subsequently, the basic of understanding on the mechanisms involved in the degradation throughout the cycling life of LIBs became a crucial focal point for the research. *In situ/operando* studies are experiments that involve monitoring the behaviour of a system under realistic operating conditions. This analysis can provide valuable insights on the aging and degradation process on the battery materials and devices. In this work, fast *in situ/operando* X-ray diffraction computed tomography experiments have been conducted on MJ1-18650 commercial cells during non-stop high C-rate cycling. The goal was to map the changes occurring in the negative electrode of an aged cell during cycling by comparing the phase transitions and lithiation distribution of electrodes in an aged cell to those in a pristine cell. Moreover, comparisons between low and high C-rates were analysed to better understand the influence of the chosen current rate on lithiation distribution inside the cell. During the experiment, the pristine cell showed a uniform phase transition across the volume, with a homogeneous lithiation distribution for both electrodes in charged and discharged states. The aged cell showed a high degree of degradation and deformation after 1200 charge/discharge cycles, with a considerable capacity loss of 14.5%. During the experiment, the aged cell showed an inhomogeneous distribution of lithiation states at both charged and discharged states. The phase transition within the electrode was affected by the rate at which current was delivered to the cell, and it was discovered that at high rates, there were many lithiation states coexisting rather than the phase transition being uniform across the volume. High discharge rates have an impact on graphite phase transitions from the cell's initial condition. The cell was considerably more impacted by current rates after ageing, exhibiting a more marked co-existence of lithiation stage across the volume. The deterioration of the cell certainly had an effect on the phase transition: the divergent dynamics between the centre of the cell and the outside body were more pronounced than in the pristine cell, and the aged cell was unable to attain a fully delithiated or lithiated state at any C rate.

[a]*Electrochemical Innovation Lab, Department of Chemical Engineering, UCL, London WC1E 7JE, UK*

[b]*The Faraday Institution, Quad One, Harwell Science and Innovation Campus, Didcot, OX11 0RA, UK*

[c]*ESRF – The European Synchrotron, 71 Avenue des Martyrs, 38000 Grenoble, France*

[d]*The ZERO Institute, University of Oxford, Holywell House, Oxford, UK. E-mail: paul. shearing@eng.ox.ac.uk*

[e]*Advanced Propulsion Lab, Marshgate, University College London, London, E20 2AE, UK*

† Electronic supplementary information (ESI) available. See DOI: https://doi.org/10.1039/d4se00358f

## Introduction

Lithium-ion batteries (LIBs) are one of the most popular power sources in consumer gadgets and electric vehicles. However, their limited lifespan presents a significant challenge. By 2025, it is predicted that 78 million batteries used to power Internet of Things (IoT) devices will be thrown away daily. An IoT device will need frequent battery replacements if its operational life is over ten years, because LIBs typically last two years or less. This issue also affects electric vehicles, where cells are generally

considered to have reached their end-of-life (EOL) once they lose 80% of their initial capacity. Therefore, understanding degradation mechanisms is crucial for enhancing the lifetime, cyclability, performance, and safety of commercial devices. As such, research has increasingly focused on fundamental insights into the processes involved in LIB deterioration throughout their cycle life. Aging and degradation processes lead to the loss of active materials at both positive and negative electrodes, in addition to the depletion of lithium inventory.[1–4]

To investigate these degradation mechanisms, various approaches have been employed, using *ex situ*, *in situ*, and *operando* techniques. *Ex situ* methods provide valuable insights into battery materials, such as structural information obtained through X-ray powder diffraction (PXRD), which reveals details about the crystalline structure of materials. PXRD is typically used to study all battery components, offering the possibility of high spatial resolution without requiring fast data acquisition. However, these methods require disassembling the battery, which risks destabilizing metastable species and exposing components to moisture and impurities. Moreover, *ex situ* methods cannot detect the dynamic behaviour of batteries operating as fully integrated systems.[5,6]

In contrast, *in situ* and *operando* techniques analyse battery materials without disassembly, under actual working conditions, providing a more comprehensive understanding of the electrochemical reactions. In particular, *operando* experiments allow for the study of kinetic and thermodynamic properties, including structural changes and intermediate states during cycling. These analyses contextualize the behaviour of materials with the device's overall performance. X-ray tomography, a non-destructive method, is particularly advantageous for studying cellular dynamics and degradation phenomena. During battery charging, lithium ions migrate from the cathode's active materials, traverse an electrolyte-saturated pore space, and enter the anode's active materials. Electrons flow through external circuitry to the anode. Analytical studies employing X-ray tomography demonstrate that lithium-ion ingress and egress cause expansion and contraction in active materials, inducing compressive stresses, deformation, and potential fractures in the electrode matrix. These effects depend on the materials used, electrode structure, and overall cell design. Over time, various mechanical, electrochemical, and thermal phenomena—including particle fractures, delamination, solid electrolyte interphase formation, lithium plating, and chemical composition changes—contribute to capacity reduction and eventual failure, which X-ray tomography can monitor.[14]

X-ray computed tomography (XCT) has become a pivotal tool for investigating LIBs, offering three-dimensional, non-destructive imaging to study internal structures and performance dynamics. XCT analyses have revealed critical insights, such as pore distributions in cathodes like NCM 811, which significantly affect ion transport and capacity under different cycling conditions. Moreover, *operando* XCT has been instrumental in examining the fracture behaviour of battery materials during electrochemical processes, elucidating the relationship between voltage and particle damage—key factors for improving battery longevity and safety.[7,8,13]

PXRD-CT (X-ray powder diffraction computed tomography) represents a significant advancement for analysing battery materials, particularly for understanding complex electrochemical processes during operation. This technique combines PXRD's material characterization capabilities with computed tomography's spatial resolution, allowing real-time monitoring of material changes during charging and discharging cycles. PXRD-CT enables researchers to analyse diffraction patterns to determine how material phases evolve during lithiation, which affects battery efficiency and capacity. It has been used to create three-dimensional images of nickel manganese cobalt (NMC) cathode electrodes, visualizing the spatial distribution of lithium ions during lithiation, and has identified reaction heterogeneity in battery electrodes during operation. Recent developments, such as pixelated energy-resolving detectors, have enhanced PXRD-CT by improving scan efficiency, reducing scan times by 42%, and increasing spatial resolution.[9–12]

The use of synchrotron facilities further enhances PXRD-CT, offering superior temporal and spatial resolution. In this work, PXRD-CT is applied to spatially map phase changes in the negative electrode of an 18 650 cell during cycling, for the first time without interrupting cycles, as was common in previous studies. Previous work demonstrated PXRD-CT's ability to reveal chemical heterogeneities in smaller cell geometries; however, larger commercial formats like the 18 650 cells have not been studied due to historically slow data acquisition rates.[15,23] This study leveraged the Extremely Brilliant Source (EBS) upgrade at the European Synchrotron Radiation Facility (ESRF). Using the high-energy ID15A beamline and a Pilatus3 X CdTe 2M detector, data were acquired in milliseconds per scan, enabling *operando* PXRD-CT of an 18 650 battery during high-rate cycling.

This study compared two LG INR18650 MJ1 cells—one pristine and one cycled 1200 times—to investigate long-term cycling degradation. PXRD-CT was used to resolve crystallographic phases in the negative electrode across 2D slices and identify capacity fade causes. Previous research demonstrated lithium distribution heterogeneities in cylindrical cells, showing regions of uniform lithiation, delayed lithiation, and inactive-to-lithiation transitions during charging.[15,36]

This study extended those findings, showing that in aged cells, graphite in the negative electrode often fails to reach fully delithiated or lithiated stages at discharge and charge ends, respectively. Mechanical deformation caused by 1200 cycles resulted in a collapsed spiral region at the cell's center, which remained partially active.

The study also investigated graphite crystallographic anisotropy, which is likely due to manufacturing processes. It was observed that the graphite *c*-axis is preferentially oriented perpendicular to the current collector foil, a configuration that can cause artifacts in tomographic reconstructions.[24–26,31,36] A novel method was proposed to mitigate these limitations by focusing on rotationally invariant scattering components.

PXRD-CT further revealed that high discharge rates exacerbate non-uniform phase transitions and lithiation stage coexistence in the electrode, effects more pronounced in aged cells.

This work marked a significant advancement in understanding the long-term cycling-induced degradation of LIBs. The temporal and spatial resolution of PXRD-CT was enhanced, allowing for high-rate cycling analyses without pausing electrochemical activity during measurements. By resolving chemical heterogeneities in aged cells and investigating the effects of aging on graphite's preferred orientation, this study advanced the methodology for studying larger format cells like the 18 650 model. With these insights, PXRD-CT emerges as a powerful tool for designing more durable, efficient, and reliable energy storage systems.

# Methodology

### Laboratory X-ray CT

The lab X-ray CT data was collected using a Nikon XT H225 (Nikon Metrology, Inc. U.S.A.) by rotating the sample through 2278 angular projections. The sample was exposed at each increment to a polychromatic X-ray beam of characteristic peak energy of 58 keV (W-K$\alpha$), each with an exposure time of 1 s; with an isotropic 36 $\mu$m reconstructed voxel length. All data was reconstructed using commercial software employing cone-beam filtered-back-projection (FBP) algorithms ("CT Pro 3D," Nikon Metrology, Inc. USA).

### Laboratory data visualisation

All lab data was visualised using Avizo Fire software (Avizo, Thermo Fisher Scientific, Waltham, Massachusetts, USA). Volume rendering and *ortho*-slice cross-sections were generated based upon the raw, unprocessed greyscale data within the tomogram.

### SEM

Scanning electron microscopy (SEM) was conducted using an EVO MA 10 SEM (Carl Zeiss, USA), operating at an accelerating voltage of 10 kV, and working distance of 7.0 mm.

### XRD-CT synchrotron set up

All synchrotron experiments were performed at the ID15A beamline 13 at the ESRF – The European Synchrotron, Grenoble, France.

### XRD-CT

XRD-CT measurements were performed with a beam energy of 100 keV and beam dimensions of 200 $\mu$m in both vertical and horizontal directions. The scattered signal was collected at rates of 250 Hz using a DECTRIS Pilatus 3X CdTe 2 M detector. The detector-sample distance was set to 1275 mm. 18 650 cells were mounted in a custom-built battery holder and connected to a Biologic SP300 potentiostat through a slip ring on the sample rotation stage. During the measurements, the sample was continuously rotated and translated at steps of 200 $\mu$m after each rotation of 360°: horizontal acquisition was large 20 mm (18 mm battery diameter + 1 mm PEEK holder), vertical acquisition was a single slice, and is therefore considered the vertical

size of the beam (200 $\mu$m). The total scan time for a dataset was 3 minutes. XRD-CT scans were performed continuously during cycling.

### Electrochemistry

Commercial LG INR18650 MJ1 cells, with a nominal capacity of 3500 mA h containing nickel-rich (LiNi$_{0.8}$Mn$_{0.1}$Co$_{0.1}$O$_2$) positive electrode and composite graphite–silicon negative electrodes were used.[35] Both pristine and aged MJ1 cells were cycled using the Biologic SP300 battery cycler.

The pristine MJ1 cell was cycled between 2.5 and 4.2 V at CC charge (C/4, 1C), CV at 4.2 V until the current dropped to 0.1 A, then OCV, followed by CC discharge (C/4, 1C, 1.5C, 2C and 3C). OCV rests of 1.5 h were made.

Commercial LG INR18650 MJ1 cells were cycled 1200 times with the following protocol: CC charge at 1.5 A to 4.2 V, CV at 4.2 V until the current dropped to 0.1 A, rest for 10 min, then CC discharge at 4 A to 2.5 V, rest for 20 min. The XRD-CT experiment was performed on the aged cell with CC charge (C/4, 1C) to 4.2 V, CV at 4.2 V until current dropped to 0.1 A, OCV, CC discharge (C/4, 1C, 1.5C, 2C and 3C). OCV rest of 1.5 h were made.

### Graphite orientation measurements

Graphite electrode orientation was measured along the radial, azimuthal and longitudinal directions: two points were selected in the battery. First the periphery of the cell was used to study the radial and longitudinal direction, and second the centre of the cell was used to study the azimuthal and longitudinal direction (Fig. 1b).

The signal from the centre and the edge of the cell was divided into 100 azimuthal sectors and integrated through pyFAI software.[32]

To investigate the crystallographic preferential orientation of the graphite electrodes, the intensities of graphite 002 reflections were extracted and plotted as a function of azimuthal angle $\eta$ (Fig. 1a). The same procedure was used on NMC 003 reflection. The process was repeated for the pristine and aged cell.

### XRD-CT reconstruction

For each measured XRD-CT slice, the 2D diffraction patterns $I(2\theta, \eta)$ from all rotational and translational positions were integrated over the azimuthal angle ($\eta$) using pyFAI software.[16] To avoid reconstruction artefacts due to graphite preferred orientation, a different approach was taken during azimuthal integration: the azimuthal range of integration was $\pm 15°$ around the vertical scattering plane, corresponding to a condition where the momentum transfer vector ($q$) is virtually parallel to the sample rotation axis ($z$) and also to the detector plane. This approach was necessary for reconstructing data with scattering components parallel to the CT rotation axis and therefore invariant for rotation. The NMC positive electrode diffraction did not show any preferred orientation and therefore was azimuthally integrated with the classic method and taken as a reference. The resulting, azimuthally integrated data was
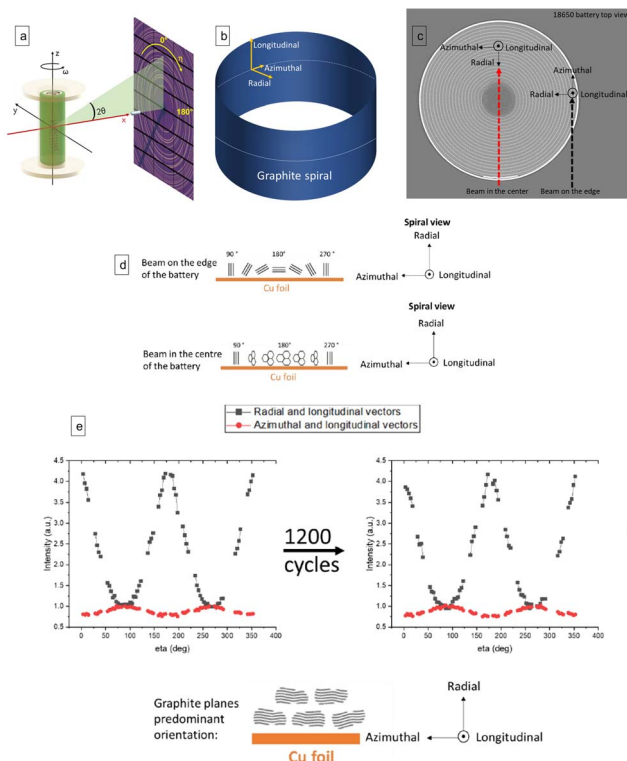
**Fig. 1** (a) Sample-detector geometry used for all experiments: the X-ray beam is directed along $x$ and normal to the detector plane; sample translation perpendicular to the beam goes along $y$; $\omega$ is the rotation angle. $\eta$ is the azimuthal angle of the powder rings acquired by the 2D detector. Adapted from ref. 36. (b) Schematic of a graphite spiral inside of an 18 650 cell and directional component used to describe the graphite preferential orientation. (c) The radial and longitudinal component of the $c$ axis orientation distribution were measured placing the X-ray beam at the periphery of the battery. The azimuthal and longitudinal components were measured placing the X-ray beam in the centre of the cell. (d) Graphite sheets orientation as a function of $\eta$ determined by the two different positions in the battery. (e left and right) The graphs represent the intensity of the 002 reflection of graphite as function $\eta$ in different planes at discharged state inside a pristine (e left) and aged (e right) 18 650 cell. The black square graphs show the intensity distribution in the plane define by the radial and longitudinal direction of pristine (e left) and aged cell (e right ). The red circle graphs show the intensity distribution in the plane defined by the longitudinal and azimuthal directions of pristine (e left) and aged cell (e right).

corrected for incident flux and sample absorption effects and finally reconstructed through an FBP algorithm implemented in Matlab (Mathworks, Cambridge, UK).[17,19]

### Rietveld refinement

Rietveld analysis was performed on each the $I(2\theta)$ patterns in each voxel in the reconstructed tomograms of the cells to calculate the weight percent of each electrode phase. Batch fit routines were set up in Topas v7 to handle the analysis of the extensive dataset.[33] The fitted model consisted of four hexagonal phases: delithiated graphite (S.G. $P6_3/mmc$), stage III (S.G. $P3$), stage II (S.G. $P6/mmm$) and stage I (S.G. $P6/mmm$) lithiated states of graphite. 2-Parameter Chebyshev polynomial

background was added to the model. Lattice parameters and scale factors were set as refinable for each phase. The peak shape was generated by refining one peak-width parameter, where the $\tan(2\theta)$-dependent broadening was convoluted with a fixed Pseudo–Voigt contribution previously refined on the calibrant powder (NIST SRM 674b $Cr_2O_3$).

### Internal phases and cell lithium distribution map

The number of moles of Li per mole of $C_6$ in the negative electrode was calculated from the mass fractions of the lithiation stages determined by Rietveld analysis.[34] The following compositions were used for each phase used for the refinement:

1. Graphite: $C_6$
2. Stage III: solid solution whose Li content varies linearly with the lattice parameter c between $LiC_{18}$ and $LiC_{30}$.
3. Stage II: $LiC_{12}$
4. Stage I: $LiC_6$

Using these compositions, the lithiation state $x$ in $Li_xC_6$ was calculated from the Rietveld refinement determined mass fractions using the following equation:

$$x = 6 \times \frac{\dfrac{\sum\limits_{s=1}^{3} m_s f_s}{w_{Li}}}{\dfrac{m_g + \sum\limits_{s=1}^{3} m_s(1 - f_s)}{w_C}}$$

Here $w_{Li}$ and $w_C$ are the atomic weights of Li and C; $m_g$ the mass fraction of graphite; $m_s$ the mass fraction of phase $s$ (lithiation stages I–III); $f_s$ the mass fraction of Li in the same phases. 18 the lithiation state $x$ in $Li_xC_6$ was calculated for each pixel in each XRD-CT scan. After the analysis 2D maps where created showing the lithiation across the cell at each time scan.

## Results

From this experiment it was possible to extract a range of information regarding the cell, including the electrode's preferential crystallographic orientation and its evolution during cycling and ageing, as well as spatially localised information of the graphite phase transition during cycling on pristine and aged cells.

### Graphite preferential orientation

The preferential orientation of the graphite electrode was analysed in both of the 18 650 (fresh and aged) cells studied in this work to determine the influence of aging on the preferential crystallographic orientation. Moreover, the analysis was carried out when the cell was both charged (graphite lithiated) and discharged (graphite delithiated) to determine the influence of SoC.

The geometry of the experiment is shown in Fig. 1a. Fig. 1b describes the different orientation directions on the electrode sheet in the battery spiral. Fig. 1c, illustrates the two positions of the X-ray beam when the measurement was conducted on the periphery and on the centre of the cell. The black dashed line

illustrates the position of the X-ray beam on the periphery of the cell to measure the distribution function of $c$-axis in the plane intersecting the radial and longitudinal directions of the electrode. The red dashed line illustrates the position of the X-ray beam when the measurement was conducted on the centre of the cell to measure the distribution function of $c$-axis in the plane intersecting the azimuthal and longitudinal directions of the electrode.

Fig. 1d illustrates the graphite sheets orientation as a function of $\eta$ in the two different positions. For example, when the beam is on the edge of the battery, thanks to the azimuthal and longitudinal direction at $\eta = 180°$ it is possible to determine the fractions of sheets to the current collector. While, when the beam is on the centre of the battery, thanks to the radial and longitudinal direction, at $\eta = 180°$ it is possible to determine the fractions of sheets perpendicular to the current collector.

Fig. 1e and f show the intensity (in a. u.) of the 002 reflection in the pristine ($e$) and cycled ($f$) cell at discharged state as function of $\eta$. The plots therefore express the statistical distribution of the orientation of the $c$-axis (normal to the graphite sheets) in different planes. The orientation of the $c$-axis in the pristine cell is primarily perpendicular to the current collector, along the radial direction, with a small fraction of $c$ axis oriented parallel to the current collector sheet.

The aging of the cell through extended cycling seems to have no influence on the graphite crystallographic orientation: the aged cell showed the same $c$-axis orientation intensity as the pristine cell. The same analysis was conducted when the cell was charged, showing the same probability distribution of $c$-axis orientation found in the discharged state (Fig. S3†).

### Degradation studies

Two 18 650 MJ1 cells were studied: pristine (after the manufacturer's formation cycles) and aged (after 1200 cycles at room temperature with CC charge at 1.5 A and CV step to 0.1 A and CC discharge at 4 A).

The pristine cell was measured as a reference for the aged cell that showed a high degree of degradation and deformation. A considerable capacity loss of 15.5% of the initial cell capacity was observed in the MJ1 cell during the aging after 1200 charge/discharge cycles (Fig. 2c). An X-ray absorption CT cross section of the 18 650 MJ1 is shown before (Fig. 2a) and after 1200 cycles (Fig. 2b). The most evident deformation after cycling is located in the central zone: the spirals have degraded, collapsing in the inner windings and modifying the tab and electrode architecture. From previous experiments, it was demonstrated that in an 18 650 cell during charge the electrodes expand outwards. However, once encountering the solid barrier that is the cell casing, the electrode has nowhere to expand but inwards, which is why the electrode deformations initiate at the core of the cell. Another useful analysis of the mechanical deformation affecting these cells is provided by Pfrang et al. It is shown the macroscopic deformation of the jelly roll in the inner layers, which causes delamination of Cu current colector from the anode caused by compressive stress. The deformation is caused by chemical/electrochemical processes and is induced by the
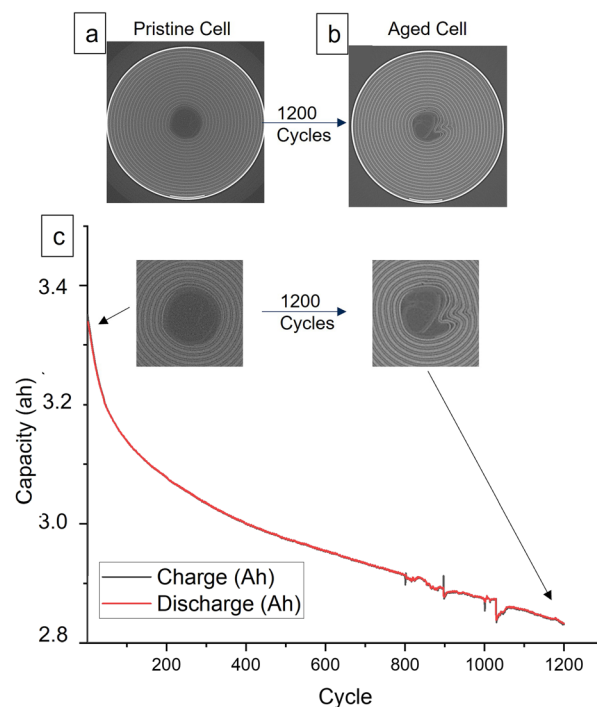


Fig. 2 (a) Absorption X-ray images of a pristine 18 650 MJ1 cell. (b) Absorption X-ray images of an 18 650 MJ1 cell cycled 1200 times. (c) Capacity fade of 18 650 MJ1 cell during 1200 cycles.

volume change of the active material in the inner layers, middle, and in the outer layers.[37] Other mechanical deformation was also shown in the study by Waldmann et al.[38] Moreover, Jnawali et al., demonstrated the greatest movement of electrodes during lithiation occurs at pre-existing inflection points in the jelly roll, which are a result of the manufacturing process, and eventually lead to the large deformations observed.[27] However, until now, the influence of this jelly-roll collapse on the cell performance and active material activity has not been quantified.[28–30]

The pristine cells reached 95.6% of the initial capacity during 1C charging. The maximum capacity is reached in 2.16 h after the CV step. The choice of cycling protocol was made to replicate normal operating condition. The aged cell with the same electrochemical protocol reached 84.4% of the initial capacity (before aging) during charge in 2.9 h after the CV step. The lower performance of the aged cell is also appreciable during discharge: the pristine cell shows 95.3% of the initial capacity in 1 h while the aged cell delivered jut 82.2% of initial capacity in 1 h.

Diffraction tomograms were acquired during electrochemical cycles in order to investigate the cause of this capacity fade. Data analysis was adapted to take into account the graphite preferential orientation discovered during the experiment. Through the analysis it was possible to evaluate the spatial distribution of degradation across the cell's volume. In addition, performance in the damaged zones in the centre of the volume was analysed to reveal the presence of inactive material. Rietveld refinement analysis was performed on pristine and aged 18 650 MJ1 cells to map lithiation inside the negative electrode across the cell during cycling.

When graphite lithiates, distinct Bragg peaks appear in the diffraction pattern. Fig. S5† shows the different lithiated states in the diffraction pattern. Lithiation inside the graphite negative electrode is calculated as shown in the Methodology section. At room temperature, and in an equilibrated state, we identified Stage III to correspond to a composition of $LiC_{30}$ and $LiC_{18}$, Stage II to $LiC_{12}$ and Stage I to $LiC_6$.[12] For this work, everything between Stage II and graphite was considered to be Stage III, and the composition of the lithium content from Stage III was estimated as a linear distribution of the $d$-spacing.[18] The estimation of $x$ in $Li_xC_6$ was determined by summing the Li content from the measured stages of lithiation during the experiment.[15] The lithiation inside the two cells is expressed through the plot of $x$ in $Li_xC_6$ across the battery volume as function of a coloured bar as shown in Fig. 3 and 4, where the fully lithiated state $LiC_6$ is represented by dark red voxels. When the volume is black, the negative electrode is in the fully delithiated state, $C_6$. The $LiC_{12}$ stage can be found at $x = 0.5$ in light green coloured voxels.

Fig. 3 shows the spatial and temporal evolution of the negative electrode lithiation of pristine and aged cells during 1C charge. Each image shows the area of the cell at a certain voltage. Fig. 3a shows the cell at the beginning of charge to be in a delithiated stage; following the charge, the fully charged state is reached in Fig. 3g. From Fig. 3a the cell appears to be in the discharged state with a 60% of voxels in $C_6$ state (black) and 32% of voxels in $Li_{0.05}C_6$ state (purple). After applying a current (3.5 A corresponding to 1C), leading to a subsequent increase in voltage, the quantity of unlithiated state ($C_6$) rapidly decreased, resulting in the formation of the lithiated graphite phases. The lithiation appeared homogenous during the cycling, reaching $LiC_{12}$ stage in 71% of the voxels at about 3.95 V during CC charge (and 24% of the voxels in $x = 0.55$), where the cell reached 41.8% of the nominal capacity. The fully lithiated $LiC_6$ stage was reached in 64% of the voxels at the end of the CV step in Fig. 3g, 32% of the voxels reached $x = 0.95$ and 2% $x = 0.9$ at the end of the charge. Therefore, the majority of the pristine cell reached $LiC_6$ state without significant heterogeneity across the volume.

The aged cell was cycled with the same cycling protocol. From Fig. 3h–n the spatial and temporal evolution of negative electrode lithiation in the aged cell during 1C charge is shown. At the beginning of charge (Fig. 3h), the aged cell is shown not to be in a fully delithiated $C_6$ state. Only 23% of the voxels display $x = 0$, while 57% of the voxels in the area shows $x = 0.05$ and 19% $x = 0.1$. This indicated that the anode does not fully delithiate in the preceding discharge step. The centre of the aged cell, where the spirals collapsed due to cycling, showed a lithium content of $0.2 < x < 0.3$, highlighting the degradation state of the area and greater evidence of 'trapped' Li propagating here.

By comparing the lithiation state of the aged cell to the pristine cell at the same voltage during charge, the aged cell had a slower phase transition and required higher voltages to start the lithiation. The $LiC_{12}$ stage was firstly detected in the outer area of the cell in 44% of the voxels at 4 V and 32.8% of theoretical capacity; while the electrode in the middle of the cell
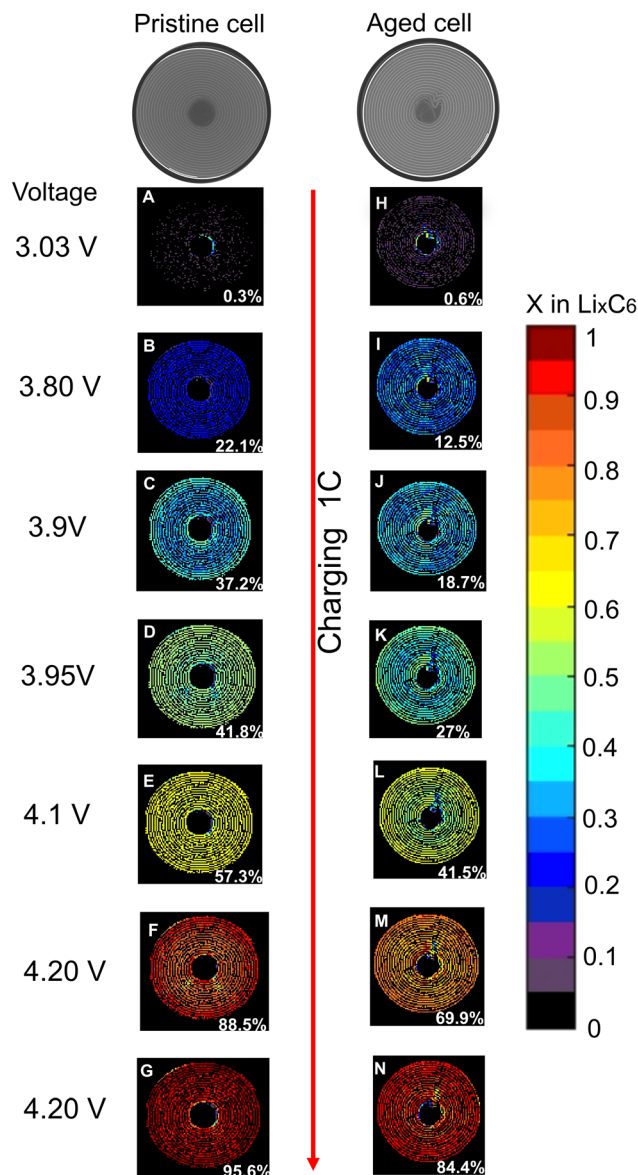


Fig. 3 Comparison of lithiation distribution inside the negative electrode in pristine (A–G) and aged cell (H–N). The lithiation distribution is analysed during a CC charge cycle at 1C for each cell. (A–N) Show the distribution of $x$ in $Li_xC_6$ as function of a coloured bar (shown on the right). Black colour corresponds to $C_6$ delithiated graphite, red colour corresponds to $LiC_6$ fully lithiated state. The voltage at which the distribution is analysed is shown on the left, while the cell capacity at which the XRD-CT corresponds is on the bottom right of each image from (A–N).

displayed in 22% of the voxels a lithiation state of $x = 0.4$ and the degraded zones, around 10% of the voxels had $x = 0.2$. At the end of the CV step, the aged cell did not reach a fully lithiated $LiC_6$ state. 25% of the voxels in the area had $x = 1$, while 71% of the voxels displayed $0.8 < x < 0.9$. The cell's damaged centre showed a lower lithiation state, with $x = 0.7$ and the most inactive zones had voxels with $x = 0.6$. Comparison of the pristine and aged cell discharge at 1C are shown in Fig. S6.†
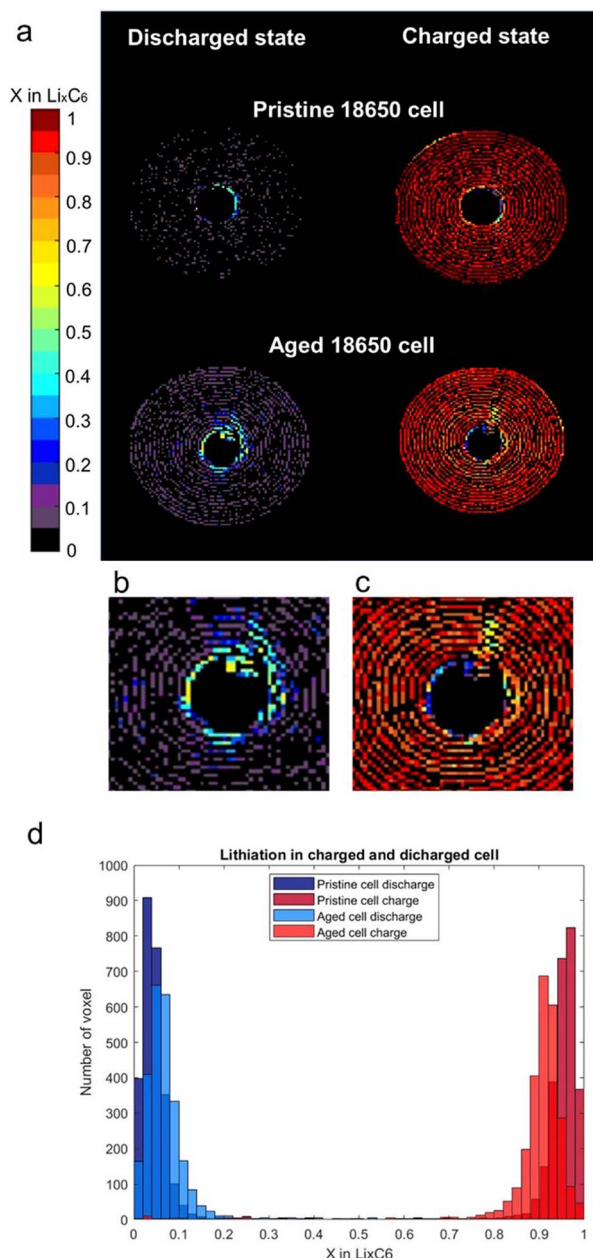
Fig. 4 (a) Comparison between pristine and aged cell at charged and discharged state. The $x$ in $Li_xC_6$ is plotted as colour bar across the volume area. (b) Zoom of aged discharged cell. (c) Zoom of aged charged cell. (d) Number of voxels vs. $x$ value in $Li_xC_6$ at discharged and full charged state of aged cell. (c) Damaged zone extended into the volume from the centre, probably derived from the spiral collapsing.

Fig. 4a shows the comparison between the pristine and aged cell at the end of a charge and at the end of a discharge. The lithiation of the graphite is plotted as before in Fig. 3 and S6† with a colour bar to show the $x$ distribution across the cells volume in the charged and discharged state. In the discharged state, the pristine cell showed a prevalence for voxels in a fully delithiated state and a few with $x = 0.05$, showing almost full reversibility of the lithiation processes. On the other hand, the aged cell was not able to reach a fully discharged state and all

the voxels show a distribution of $x = 0.05, 0.1, 0.15$. Moreover, at the centre of the aged cell there is a mixture of $x = 0.5, 0.45, 0.4$. In the charged state, the pristine cell showed a homogenous fully charged state distribution, while the aged cell shows an inhomogeneous distribution of $x = 0.8, 0.85, 0.9$. In this case, the centre of the aged cell shows a distribution of $x$ between 0.2 and 0.6, indicating a multiplicity of lithiation states between $LiC_{30}$ and $LiC_{12}$. The aged cell lithiation during charge demonstrated a general loss of activity in the cell's centre.

The different lithiation distributions of the pristine and aged cells in the discharged and charged state is shown in Fig. 4b where the number of voxels containing a certain $x$ in $Li_xC_6$ are plotted as a bar chart for both cells. The aged cell showed a broader distribution of lithiation states, highlighting the fact that after multiple cycles there is a decrease in the cell capacity and efficiency across the negative electrode.

To understand the degradation of graphite and its influence on the cell performance, the capacity of the negative electrode was evaluated by calculating the overall lithiation states for both the pristine and aged cells in the charged state (Table 1). The fully lithiated $LiC_6$ ($x = 1$) was correlated to the 3.5 A h theoretical capacity of the cell. The graphite capacity at charged state for the pristine and aged cell was calculated by proportional dependence of the $x$ obtained from the Rietveld refinement, with the $x = 1$ corresponding to 3.5 A h theoretical capacity.

The capacity of the negative electrode decreased after the ageing process and the experiment by 8.8%. After aging, from electrochemical cycling, the entire cell capacity decreased by 14%. The degradation of the graphite negative electrode does not explain the entire capacity fade of the aged cell. Other causes can be found in the degradation of the positive electrode, loss of electrical contact due to spiral collapse and delamination, and degradation of electrolyte.

The analysis has shown that the phase transition was not homogenous across the area of the cell. In particular, the centre of the volume where the collapsed spirals were identified (from absorption tomography), appeared to be significantly less active. The lithiation at the centre of the cell was slower and incomplete when compared to the outer area. In particular, the centre of the aged cell showed deactivation and loss of active material due to the physical deformation of the cell after long term cycling. However, it was demonstrated that the damaged zone, where the spirals collapsed was still partially active. Another degraded zone inside the area of the aged cell was

Table 1 Graphite electrode capacity degradation. For both cells, all the intensities of the diffractogram at certain time corresponding to the charged state were summed up across the cell volume. The obtained diffractograms were refined with Rietveld refinement and $x$ in $Li_xC_6$ was calculated (second column). By relating $x = 1$ to 3.5 A h of nominal capacity of the cell, the graphite capacity was calculated for both cells (third column)

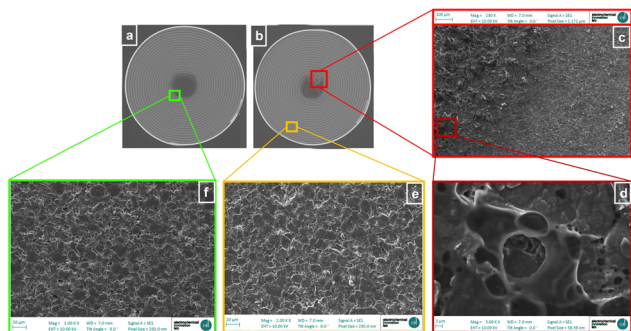| Charged state | Lithiation state ($x$ in $Li_xC_6$) | Capacity (A h) of graphite |
|---|---|---|
| Pristine | 0.939 | 3.28 |
| Aged | 0.8547 | 2.99 |

**Fig. 5** (a) Absorption tomography of pristine cell. (b) Absorption tomography of aged cell (c) and (d). Show multi-scale view of the heavily deformed zone of the aged cell centre. (e) Standardised SEM image before cycling. (f) Standardised SEM image after cycling.

detected from the collapsed spirals going radially inside the area of the cell (Fig. 4c), suggesting that the damage was extended from the centre of the cell to the body.

After cell disassembly, the materials were investigated further using scanning electron microscopy (SEM). SEM images of the aged negative electrode from both the cell centre and exterior windings were acquired (Fig. 5d and c respectively). For comparison, SEM images of the pristine cell negative electrode were also acquired (Fig. 5e). As shown in Fig. 5d a formation of a thick surface layer completely covering the negative electrode in the centre of the aged cell was observed. This extensive surface layer formation was detected only in the damaged area of the aged cell centre, and may be consistent with excessive local SEI formation and consequently another cause of the lower performance of the cell in that region.

The graphite phase transition was also studied in both the pristine and aged cells at different discharge rates, to determine the influence of the C-rate on the lithiation of the negative electrode. Fig. 6a–c show the weight% of each phase inside the negative electrode of the pristine cell during discharge at different current rates. During the discharge of the pristine cell at 0.5C, the entire cell area gradually changed lithiation state from $LiC_6$ to $C_6$. When the pristine cell underwent a 1C discharge the lithiation states were more broadly distributed: the external region preferentially lithiates with respect to the centre of the cell. Moreover, there was a broad distribution of lithiation stages at the same time. This behaviour was more pronounced when a 2C discharge rate was applied: the lithiation state distribution within the cell area is broader, with more lithiation stages simultaneously present at the same voltage in the same voxel.

Fig. 6d–f show the weight% of phase during discharge with different C-rates used with the aged cell. During the discharge at 0.5C, the entire cell area gradually changed lithiation state from $LiC_6$ to $C_6$. However, the phase transition was not homogenous across the volume. A slower transition in the centre than at the outer body was observed. When a 1C discharge rate is applied to the aged cell, the lithiation states were more broadly distributed. The distribution of lithiation state at a given time indicates a slower kinetics. This behaviour was further pronounced when a 2C discharge rate was applied with an even more
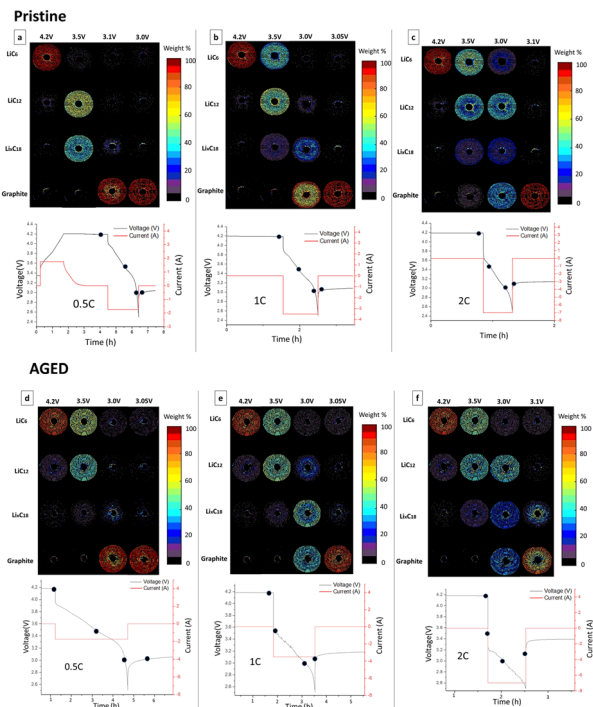


**Fig. 6** Weight% distribution of different graphite phases during discharge at increasing C rates inside the pristine cell. Pristine cell is showed in (a)–(c), starting from a C rate of 0.5 to 2C. Aged cell is showed in (d)–(f), starting from a C rate of 0.5 to 2C.

pronounced heterogeneity of lithiation stages across the volume. Moreover, the aged cell did not reach the fully delithiated stage in all the voxels at the end of discharge. At each current, numerous voxels showed a 10% concentration of $LiC_6$ phase at the end of the cycle. At high rates, in particular at 2C, the aged cell also showed that numerous voxels did not transition fully to graphite (during discharge), remaining partially lithiated in the $Li_xC_{18}$ state. This phenomenon was particularly present in the centre of the cell in the region affected by mechanical deformation.

The current applied to the cell influenced the phase transition inside the electrode, revealing that at higher currents, the phase transition was less homogeneous across the volume, but there was a coexistence of multiple lithiation stages. High rates of discharge affected graphite phase transitions from the pristine state of the cell. After ageing, the cell was even more affected by high current, showing a more pronounced coexistence of lithiation states across the volume. The degradation of the cell clearly had an influence the phase transition: the different dynamics between centre of the cell and outer body is more accentuated compared with the pristine cell, and the cell was not capable of reaching a fully delithiated state.

## Conclusions

Synchrotron XRD-CT measurements can help in investigating degradation processes in batteries by providing spatially resolved diffraction patterns of a battery during operation as a function of time. This technique enables *in situ* and *operando*

insights of an electrochemical cell, which can elucidate the degradative pathways occurring during long-term operation. For the first time, fast XRD-CT was be used to map phase changes in the negative electrode of an 18 650 cell while the battery was cycled with high C-rates, and to evaluate the spatial distribution of degradation across the cell's volume. In addition, performance in the damaged zones in the centre of the volume can be analysed to reveal the performance, the presence of inactive material and loss of electrical contact. The aging mechanism in 18 650 cells involves a loss of active materials at both positive and negative electrodes, as well as lithium inventory loss. This aimed to illustrate the changes occurring in the volume of an aged cell during cycling by comparing the phase transitions and lithiation distribution of negative electrodes in an aged cell to those in a pristine cell. The 18 650 cell was chosen because of its commercial relevance, providing a case study to explore the degradation mechanism in a full commercial device without disassembly. The aim was to spatially resolve crystallographic phases and their evolution during cycling, in particular to map the phase transition of the negative electrode across the cell volume. After 1200 cycles, the most evident deformation after cycling is located in the central zone: the spirals have degraded, collapsing in the inner windings and modifying the tab and electrode architecture and the cell was at 80% SoC.

The capacity of the negative electrode was evaluated by calculating the overall lithiation states for both the pristine and aged cells in the charged state. The results showed that the aged cell had a lower capacity than the pristine cell, indicating that the graphite electrode had degraded over time. The study also aimed to spatially resolve crystallographic phases and their evolution during cycling, in particular to map the phase transition of the negative electrode across the cell volume. Rietveld refinement analysis was performed on pristine and aged cells to map lithiation inside the negative electrode across the cell during cycling. The results showed that the phase transition was not homogeneous across the volume, with a slower transition in the centre than in the outer body. The tab located in outside the jelly roll in the cell seems to not have an influence on the states transition during cycling. However, the different mechanical stress at the centre of the cell acting like as starting point of the mechanical deformation,[20] also influenced the state transitions inside the negative electrode. Additionally, the distribution of lithiation state at a given time indicated the loss of capacity of the active material.[21,22]

The influence of current rate on the phase transition of the negative electrode was studied in both the pristine and aged cells at different discharge rates to determine the influence of the C-rate on the lithiation of the negative electrode. The rate of current applied to the cell influenced the phase transition inside the electrode, revealing that at high rates, the phase transition was not homogeneous across the volume, but there was a coexistence of multiple lithiation states. High rates of discharge affected graphite phase transitions from the pristine state of the cell. After aging, the cell was even more affected by current rates, showing a more pronounced co-existence of lithiation stage across the volume. The degradation of the cell

clearly had an influence on the phase transition: the different dynamics between the centre of the cell and outer body were more accentuated compared with the pristine cell, and the cell was not capable of reaching a fully delithiated state.

These findings provide insights into the degradation mechanisms of lithium-ion batteries and highlight the importance of developing strategies to mitigate the effects of cycling-induced degradation on battery performance and lifespan. Future work could include improving the resolution and sensitivity of XRD-CT techniques to enable more detailed mapping of phase transitions and degradation mechanisms in lithium-ion batteries. XRD-CT maps can be also used to evaluate the spatial distribution of positive electrode degradation across the cell's volume, and can be readily applied to next generation battery chemistries.[39,40] Additionally, future work could explore the use of XRD-CT in combination with other analytical techniques, such as neutron scattering, electron microscopy and spectroscopy, to provide a more comprehensive understanding of the structural and chemical changes that occur during battery cycling.

## Data availability

Data are available upon request from the authors. A large quantity of data was generated in the course of these experiments which has not yet been archived in a publicly accessible repository. The authors are exploring this currently whilst the revised paper is in review.

## Author contributions

IM led the investigation. IM, TH, MM, PS conceived the experiments. TH, IM, CT, SC, MM, MJ, AJ, performed the experiments, IM, SC, MM, MJ, performed the data analysis. MM leads work at ESRF as the Scientist in Charge of ID15A. RJ leads work as the Degradation Project Manager for the Faraday Institution. AR contributed to supervision. PS and DB lead all work from the Electrochemical Innovation Lab (UCL) and sourced all funding to support this work.

## Conflicts of interest

There are no competing interests known to the authors to declare.

## Acknowledgements

# Notes and references

1 https://www.enables-project.eu/.

2 D. P. Finegan, In-operando high-speed tomography of lithium-ion batteries during thermal runaway, *Nat. Commun.*, 2015, **6**, 6924.

3 C. R. Birkl, M. R. Roberts, E. McTurk, P. G. Bruce and D. A. Howey, Degradation diagnostics for lithium ion cells, *J. Power Sources*, 2017, **341**, 373–386.

4 M. Broussely, *et al.*, Main aging mechanisms in Li ion batteries, *J. Power Sources*, 2005, **146**, 90–96.

5 D. Matras, T. E. Ashton, H. Dong, M. Mirolo, I. Martens, J. Drnec, J. A. Darr, P. D. Quinn, S. D. M. Jacques, A. M. Beale and A. Vamvakeros, Emerging chemical heterogeneities in a commercial 18650 NCA Li-ion battery during early cycling revealed by synchrotron X-ray diffraction tomography, *J. Power Sources*, **539**, 2022.

6 J. Asenbauer, *et al.*, The success story of graphite as a lithium-ion anode material-fundamentals, remaining challenges, and recent developments including silicon (oxide) composites, *Sustain. Energy Fuels.*, 2020, **4**, 5387–5416.

7 B. Pan, Y.-G. Lee, X. Wu and J. Whitacre, Micrometer Scale X-ray CT-Informed Optimization of Heterogeneous Pore Distribution in Double Layered Thick LiNCM 811 Cathode, *J. Electrochem. Soc.*, 2024, **171**, 070513.

8 H. Parks, M. Jones, A. Wade, A. Llewellyn, C. Tan, H. Reid, *et al.*, Non-Linear Damage Response to Voltage Revealed by Operando X-ray Tomography in Polycrystalline NMC811, *ChemRxiv*, 2024, preprint, DOI: 10.26434/chemrxiv-2024-npkvm-v3.

9 T.-T. Nguyen, J. Xu, Z. Su, *et al.*, 3D Operando Monitoring of Lithiation Spatial Composition in NMC Cathode Electrode by X-ray Nano-CT & XANES Techniques, *Microsc. Microanal.*, 2022, **28**(S1), 194–196, DOI: 10.1017/S1431927622001659.

10 H. Liu, S. Kazemiabnavi, A. Grenier, G. Vaughan, M. Di Michiel, B. J. Polzin, K. Thornton, K. W. Chapman and P. J. Chupas, *ACS Appl. Mater. Interfaces*, 2019, **11**(20), 18386–18394.

11 D. Schröder, *et al*, *J. Phys. D: Appl. Phys.*, 2016, **49**, 404001.

12 A. Ajeer, J. C. Khong, M. D. Wilson and R. M. Moss, Hybrid energy and angle dispersive X-ray diffraction computed tomography, *Opt. Express*, 2023, **31**, 12944–12954.

13 S. Dayani, H. Markötter, A. Schmidt, M. P. Widjaja and G. Bruno, Multi-level X-ray computed tomography (XCT) investigations of commercial lithium-ion batteries from cell to particle level, *J. Energy Storage*, 2023, **66**, 107453.

14 P. Pietsch and V. Wood, X-ray tomography for lithium ion battery research: a practical guide, *Annu. Rev. Mater. Res.*, 2017, **47**(1), 451–479.

15 D. Matras, T. E. Ashton, H. Dong, M. Mirolo, I. Martens, J. Drnec, J. A. Darr, P. D. Quinn, S. D. M. Jacques, A. M. Beale, A. Vamvakeros,.

16 D. Liu, *et al.*, Review of Recent Development of In Situ/Operando Characterization Techniques for Lithium Battery Research, *Adv. Mater.*, 2019, **31**, 1–57.

17 K. M. Ø. Jensen, *et al.*, X-Ray Diffraction Computed Tomography for Structural Analysis of Electrode Materials in Batteries, *J. Electrochem. Soc.*, 2015, **162**, A1310–A1314.

18 H. Liu, *et al.*, Quantifying Reaction and Rate Heterogeneity in Battery Electrodes in 3D through Operando X-ray Diffraction Computed Tomography, *ACS Appl. Mater. Interfaces*, 2019, **11**, 18386–18394.

19 S. R. Daemi, *et al.*, Exploring cycling induced crystallographic change in NMC with X-ray diffraction computed tomography, *Phys. Chem. Chem. Phys.*, 2020, **22**, 17814–17823.

20 D. P. Finegan, *et al.*, Spatially Resolving Lithiation in Silicon-Graphite Composite Electrodes *via in situ* High-Energy X-ray Diffraction Computed Tomography, *Nano Lett.*, 2019, **19**, 3811–3820.

21 V. Vanpeene, A. King, E. Maire and L. Roué, In situ characterization of Si-based anodes by coupling synchrotron X-ray tomography and diffraction, *Nano Energy*, 2019, **56**, 799–812.

22 D. Petz, *et al.*, Lithium distribution and transfer in high-power 18650-type Li-ion cells at multiple length scales, *Energy Storage Mater.*, 2021, **41**, 546–553.

23 P. Raimondi, *et al.*, The Extremely Brilliant Source storage ring of the European Synchrotron Radiation Facility, *Commun. Phys.*, 2023, **6**, 82.

24 P. Baade, *et al.*, Rapid, Non-Invasive Method for Quantifying Particle Orientation Distributions in Graphite Anodes, *J. Electrochem. Soc.*, 2017, **164**, E348.

25 S. Malifarge, *et al.*, Quantification of preferred orientation in graphite electrodes for Li-ion batteries with a novel X-ray-diffraction-based method, *J. Power Sources*, 2017, **343**, 338e344.

26 M. D. R. Kok, *et al.*, Virtual unrolling of spirally-wound lithium-ion cells for correlative degradation studies and predictive fault detection, *Sustain. Energy Fuels.*, 2019, **3**(11), 2972–2976.

27 A. Jnawali, A. N. P. Radhakrishnan, M. D. R. Kok, F. Iacoviello, D. J. L. Brett and P. R. Shearing, Motion-enhancement assisted digital image correlation of lithium-ion batteries during lithiation, *J. Power Sources*, 2022, **527**, 231150.

28 C. Meyer, *et al.*, Characterization of the calendering process for compaction of electrodes for lithium-ion batteries, *J. Mater. Process. Technol*, 2017, **249**, 172–178.

29 W. Haselrieder, *et al.*, Impact of the Calendering Process on the Interfacial Structure and the Related Electrochemical Performance of Secondary Lithium-Ion Batteries, *ECS Trans.*, **50**(26), 59–70.

30 R. Sim, *et al.*, Influence of Calendering on the Electrochemical Performance of $LiNi_{0.9}Mn_{0.05}Al_{0.05}O_2$ Cathodes in Lithium-Ion Cells, *ACS Appl. Mater. Interfaces*, 2021, **13**(36), 42898–42908.

31 Z. Du, *et al.*, High Energy Density Calendered Si Alloy/Graphite Anodes, *J. Electrochem. Soc.*, 2014, **161**, A1698.

**Sustainable Energy & Fuels**

View Article Online

Paper

32 G. Ashiotis, *et al.*, The Fast Azimuthal Integration Python Library: PyFAI, *J. Appl. Crystallogr.*, 2015, **48**(2), 510–519.

33 A. Coelho, TOPAS and TOPAS-Academic: an optimization program integrating computer algebra and crystallographic objects written in C++, *J. Appl. Crystallogr.*, 2018, **51**, 210–218.

34 D. Finegan, *et al.*, Spatial dynamics of lithiation and lithium plating during high-rate operation of graphite electrodes, *Energy Environ. Sci.*, 2020, **13**, 2570–2584.

35 M. M. Heenan, A. Jnawali, M. D. R. Kok, G. Tranter, C. Tan Dimitrijevic, R. Jervis, D. J. L. Brett and P. R. Shearing, An Advanced Microstructural and Electrochemical Datasheet on 18650 Li-Ion Batteries with Nickel-Rich NMC811 Cathodes and Graphite-Silicon Anodes, *J. Electrochem. Soc.*, 2020, **167**, 140530.

36 T. M. M. Heenan, I. Mombrini, A. Llewellyn, *et al.*, Mapping internal temperatures during high-rate battery applications, *Nature*, 2023, **617**, 507–512, DOI: **10.1038/s41586-023-05913-z.**

37 A. Pfrang, A. Kersys, A. Kriston, R.-G. Scurtu, M. Marinaro and M. Wohlfahrt-Mehrens, Deformation from Formation Until End of Life: Micro X-ray Computed Tomography of Silicon Alloy Containing 18650 Li-Ion Cells, *J. Electrochem. Soc.*, 2023, **170**, 030548.

38 T. Waldmann, *et al.*, A Mechanical Aging Mechanism in Lithium-Ion Batteries, *J. Electrochem. Soc.*, 2014, **161**, A1742.

39 L. Q. Mai, *et.al.*, Engineering d-p Orbital Hybridization with P, S Co-Coordination Asymmetric Configuration of Single Atoms Toward High-Rate and Long-Cycling Lithium–Sulfur Battery, *Adv. Mater.*, 2024, **36**, 2407070.

40 L. Q. Mai, *et.al.*, A Highly Stable and Non-Flammable Deep Eutectic Electrolyte for High-Performance Lithium Metal Batteries, *Angew. Chem.*, 2024, **63**, e20241122.